Computational Particle Mechanics 15 (2026) 226–246

Contents lists available at ScienceDirect

Computational Particle Mechanics

journal homepage: www.sciencedirect.com/journal/computational-particle-mechanics

A nested SPH approach for simulating propeller jet wakes over scoured bathymetry☆

D. Ferraro [a],*, J.M. Domínguez [b], A. Lauria [c], C. Altomare [d], R. Gaudio [a], F. Aristodemo [a]

[a] Department of Civil Engineering, University of Calabria, Ponte P. Bucci, 42B, Rende, 87036, Italy
[b] Environmental Physics Laboratory, CIM-UVIGO, University of Vigo, Rúa Canella da Costa da Vela, 12, Ourense, 32004, Spain
[c] Department of Engineering for Innovation, University of Salento, Strada Provinciale, 6, Lecce, 73100, Italy
[d] Maritime Engineering Laboratory LIM-UPC, Polytechnic University of Catalonia, Campus Diagonal Nord, Building D1, Barcelona, 08034, Spain

ARTICLE INFO

Keywords:
SPH
Nesting strategy
Multiscale hydrodynamics
Propeller jet

ABSTRACT

This work presents a numerical investigation of the three-dimensional hydrodynamics generated by a propeller jet (PJ) operating above a scoured bathymetry (SB), a configuration frequently encountered in harbour basins and navigable waterways where propeller-induced flows lead to local bed erosion. Accurately modelling the interaction between the propeller jet, the equilibrium scour geometry, and the surrounding flow field remains computationally demanding, due to the coexistence of highly localised turbulent structures and the large spatial scales typical of laboratory and field settings.

To address this multiscale challenge, a nesting strategy is developed within the Smoothed Particle Hydrodynamics (SPH) framework. The approach couples a high-resolution SPH domain, dedicated to resolving the near-field hydrodynamics of the propeller jet, with a larger domain discretised at coarser resolution, representative of the overall experimental environment. This formulation enables an efficient transfer of flow information across scales, substantially reducing computational costs while retaining the essential dynamics of the jet–bathymetry interaction.

The numerical model is validated against laboratory measurements obtained under steady current conditions, showing good agreement in terms of velocity distributions, jet spreading, and flow structures influenced by the scoured bed. Additional simulations under still-water and regular-wave conditions further demonstrate the robustness of the proposed methodology. Overall, the results confirm the suitability of the nested SPH approach for simulating fully three-dimensional propeller-induced flows interacting with complex bed geometries.

1. Introduction

The reproduction of the hydrodynamics generated by propellers is fundamental for improving vessel performance, reducing fuel consumption, and mitigating environmental impacts. The flow produced by a rotating propeller is inherently three-dimensional, dominated by strong axial, tangential, and radial components, and characterised by the formation and evolution of coherent vortical structures such as tip and root vortices (e.g., [1–3]). These features govern momentum transport, turbulence generation, and the

☆ This article is part of a Special issue entitled: 'CPMS_SPHERIC' published in Computational Particle Mechanics.

* Corresponding author.
E-mail address: domenico.ferraro@unical.it (D. Ferraro).

https://doi.org/10.1016/j.cpms.2026.05.002
Received 2 March 2026; Received in revised form 24 April 2026; Accepted 2 May 2026
Available online 12 May 2026

near- and far-field behaviour of the PJ, with important implications on scour and deposition processes, sediment resuspension, and ship-seabed interactions [1].

Historically, the seminal work by Albertson et al. [4] provided the first analytical interpretation of submerged jets, identifying the establishing and established flow zones, which still serve as reference conceptual models. More recent laboratory investigations using Laser Doppler Anemometry (LDA), Acoustic Doppler Velocimetry (ADV), and Particle Image Velocimetry (PIV) have refined the understanding of the bimodal velocity distribution in the near field, driven by the hub wake deficit and blade-induced velocity peaks (e.g., [3,5]). These studies confirm the complexity of the velocity field and the persistence of helical vortical structures in the wake, which contribute to anisotropic turbulence and helicity generation [1].

In parallel with experimental efforts, Computational Fluid Dynamics (CFD) techniques have become central to the investigation of propeller-induced flows. Finite Volume Methods (FVM) employing Reynolds-Averaged Navier–Stokes Equations (RANSE), Detached Eddy Simulation (DES), and Large Eddy Simulation (LES) have been extensively used to reproduce the hydrodynamics of PJs (e.g., [2,6,7]). LES- and DES-based approaches have successfully captured wake instabilities, tip vortex breakdown, and turbulence generation mechanisms far downstream, making them the current standard for high-fidelity propeller simulations. Nevertheless, the RANSE approach remains widely adopted, owing to its computational efficiency, despite known dissipation issues and limitations in resolving small-scale turbulent structures [8].

In recent years, mesh-free Lagrangian methods have emerged as an alternative to traditional Eulerian mesh-based solvers. Among others, SPH offers advantages for problems involving large deformations, moving boundaries, and free surfaces, and has been extensively applied in river, coastal, and offshore engineering (e.g., [9–11]). However, applications of SPH in simulating propeller-induced flows remain marginal. The first study refers to Ulrich et al. [12], who reproduced the propeller geometry by a simple cylindrical actuator disk to study rapid bed erosion processes. However, the true hydrodynamics induced by the rotating blades of the propeller was not simulated. More recently, SPH has been successfully compared with high-fidelity FVM simulations in PJ flows, demonstrating its capability to capture three-dimensional velocity fields, vorticity structures, and time–frequency turbulence signatures [13]. The analyses were limited to the near field, owing to the heavy computational effort driven by the thin complex geometry of the propeller.

While mesh-based approaches (RANSE/LES/DES) rely on well-established turbulence models and offer high computational efficiency for large domains, they face challenges such as grid distortion near moving blades and limitations in representing highly deformable free surfaces. In contrast, SPH naturally handles moving boundaries, multiphase flows, and fluid–structure interactions, making it particularly suitable for complex bathymetries and, in future, for modelling long-term sediment transport processes related to the achievement of equilibrium scour and deposition configurations.

Despite these advances, several challenges still hinder the application of SPH to PJ studies, including a realistic bed and large domains. In this context, Ferraro et al. [14] emphasised the importance of reproducing the interaction between propeller jets, waves, and evolving bathymetry in realistic-scale environments, showing that the hydrodynamics around a scoured bed differ substantially from that over a flat plane. Likewise, the evolution of helical turbulence in propeller wakes suggests that accurate near-blade resolution is critical for reproducing vortex generation and dissipation [1]. As a result, a suitable simulation requires an accurate resolution of the near-field flow around the propeller, which is computationally expensive, and a sufficient resolution to model a larger domain and capture well the far-field. This mismatch between near and far spatial scales can motivate the use of variable-resolution strategies. While such multi-scale approaches are common in mesh-based CFD, such as overset grids or local mesh refinement (e.g., [15]), they have only recently begun to be explored within mesh-free Lagrangian frameworks by multi-node strategy [16], domain nesting techniques [17], or local particle refinement for two-dimensional [18] and three-dimensional [19] simulations.

Besides, SPH still suffers from high computational cost at fine resolution, incomplete turbulence modelling frameworks at high Reynolds numbers, and challenges in enforcing boundary conditions for rotating systems. To address these issues, recent research has focused on enhancing numerical fidelity through schemes such as Optimised Particle Shifting (OPS), Velocity divergence Error Mitigating (VEM), and Volume Conservation Shifting (VCS), which have been prominently integrated into the DualSPHysics+ branch [20]. These advancements represent the current state-of-the-art for improving stability and volume preservation in complex SPH simulations. Nevertheless, the recent study by Ferraro et al. [13] shows that SPH can reproduce velocity and vorticity fields comparable to LES-FVM, including tip vortex signatures and helical structures, highlighting its potential for high-fidelity PJ simulation when supported by efficient computational strategies.

Owing to the lack of SPH studies resolving propeller hydrodynamics over realistic scoured topographies, there is a clear need for numerical strategies capable of bridging near-field jet dynamics and large-scale environmental domains. This work addresses this gap by developing a nesting strategy within an SPH framework that embeds a high-resolution inner domain around the propeller within a larger, lower-resolution outer domain reproducing laboratory-scale flume conditions. This approach enables a reliable modelling of PJ wake evolution and its interaction with scoured bathymetry, while significantly reducing computational cost. In this framework, the proposed nesting strategy, while building upon established SPH components like the MESH-IN technique [17] and Relaxation Zone [21], introduces original methodological adaptations. A key departure from standard applications is the implementation of localised internal nesting, in which the high-resolution propeller-induced jet is directly imposed within a specific fluid region of the coarser domain. Furthermore, a periodic embedding strategy is developed to cyclically impose the 3D velocity signature. This approach ensures that the dominant unsteady wake structures and the blade-passage signature are accurately preserved until a statistically steady hydrodynamic state is reached, avoiding the prohibitive computational cost of full-blade simulations for the entire duration.

The proposed strategy is validated against laboratory experiments in the presence of a steady open-channel flow. Afterwards, numerical cases in still water conditions and involving the superimposition of regular waves are exploited through the current approach.

The present work is organised as follows. Section 2 describes the SPH solver used, paying attention to the computational techniques and the novel nesting strategy. In Section 3 experimental set-ups and measurement procedures are presented. Section 4 illustrates the numerical results. In particular, Section 4.1 shows the model validation for the test case with the ambient current, whereas the subsequent Sections 4.2 and 4.3 highlight numerical results in still water conditions and in the presence of regular waves. Finally, Conclusions close the article.

2. DualSPHysics model

DualSPHysics is a numerical solver based on the SPH method, specifically designed to exploit modern parallel hardware such as multicore CPUs and NVIDIA GPUs. Its parallel architecture enables the simulation of a relevant number of particles with reduced computational cost, providing a robust platform for modelling complex free-surface and turbulent flows. The SPH-based code is built upon a weakly compressible assumption and includes coupling interfaces with external multiphysics engines such as Discrete Element Method, Project Chrono, and MoorDynPlus, enabling advanced fluid–structure and fluid-solid interaction simulations [22]. In this work, the DualSPHysics solver (v5.4) was used to model the hydrodynamics of a PJ over a scoured bathymetry, integrating an artificial (numerical) closure scheme and a turbulence closure model, different boundary conditions, and a dedicated nesting strategy tailored for multi-scale modelling.

2.1. Governing equations

SPH method discretises the Navier–Stokes equations in Lagrangian form. A generic function F is approximated in discrete form using kernel interpolation as follows

$$F(\mathbf{r}_a) = \sum_b F(\mathbf{r}_b) W(\mathbf{r}_a - \mathbf{r}_b, h) \frac{m_b}{\rho_b}, \tag{1}$$

where $\mathbf{r}$ is the generic position, a and b are the subscripts associated with the target and the neighbour particles, respectively, W is the kernel function, h is the smoothing length, and m_b and ρ_b are the mass and density of neighbour particles, respectively. The smoothing length was evaluated as $h = c_h \sqrt{3d_p^2}$, where the coefficient c_h was set to 1.2 for all simulation cases, while d_p represents the initial interparticle distance. Among the available kernels, we use a Quintic Wendland kernel [23], preferred for increased stability and reduced particle disorder [24].

The continuity equation is written as

$$\frac{d\rho_a}{dt} = \rho_a \sum_b m_b \frac{1}{\rho_b} (\mathbf{v}_{ab} \cdot \nabla_a W_{ab}) + D_a, \tag{2}$$

where ρ_a is the target particle density, t is the time, the operator $(\cdot)_{ab}$ is given as $(\cdot)_a - (\cdot)_b$, $\mathbf{v}$ is the velocity vector, and D_a is a diffusive term included to reduce high-frequency pressure oscillations (see, for more details, [25]). While recent developments in DualSPHysics include advanced numerical schemes aimed at reducing acoustic noise and pressure oscillations in weakly compressible SPH formulations (see [26]), their assessment lies beyond the scope of the present study. Future work will address the potential benefits of these approaches in complex three-dimensional applications.

The momentum equation is here written to include a generic dissipation term $\boldsymbol{\Gamma}_a$, which will be specified hereinafter. It reads as

$$\frac{d\mathbf{v}_a}{dt} = -\sum_b m_b \left(\frac{p_a + p_b}{\rho_a \rho_b} \right) \nabla_a W_{ab} + \boldsymbol{\Gamma}_a + \mathbf{g}, \tag{3}$$

with p the pressure and $\mathbf{g}$ the gravitational acceleration. The anti-symmetric momentum-conservative formulation adopted in Eq. (3) ensures strict linear momentum preservation. While this scheme is inherently susceptible to Tensile Instability (TI) [27,28], the stability is here managed through the use of the high-order Wendland kernel and the Particle Shifting Technique (PST) described below. The implementation of specific Tensile Instability Control (TIC) schemes, such as the δ^+-SPH framework [27], extended high-order modelling [29], or transport velocity formulations [30], presents non-trivial challenges when coupled with multiscale nesting interfaces [31]. Furthermore, although other solvers derived from DualSPHysics, such as DualSPHysics+ [20], developed from DualSPHysics v5.2, have successfully integrated advanced TIC algorithms (e.g., [27]), these features are not included in the official core of DualSPHysics v5.4 used in the present work. Therefore, the strictly momentum-preserving approach was preferred to ensure robustness at the inter-domain boundaries.

In a first canonical approach implemented in DualSPHysics, $\boldsymbol{\Gamma}_a$ is modelled by an artificial viscosity [32] given by

$$\prod_{ab} = \begin{cases} \dfrac{-\alpha \overline{c_{ab}}\, h\, \mathbf{v}_{ab} \cdot \mathbf{r}_{ab}}{\overline{\rho_{ab}} \left(r_{ab}^2 + 0.01 h^2 \right)} & \mathbf{v}_{ab} \cdot \mathbf{r}_{ab} < 0, \\ 0 & \mathbf{v}_{ab} \cdot \mathbf{r}_{ab} > 0, \end{cases} \tag{4}$$

where $\overline{c_{ab}}$ (mean speed of sound) = $0.5(c_a+c_b)$, $\mathbf{r}_{ab} = \mathbf{r}_a - \mathbf{r}_b$, and $\overline{\rho_{ab}}$ (mean density) = $0.5(\rho_a+\rho_b)$. The artificial viscosity coefficient α needs to be tuned in order to introduce a proper dissipation and is usually set to 0.01 for fluid-solid interaction problems (e.g., [9]).

A second type of dissipation term developed in DualSPHysics involves the laminar viscosity and the Sub-Particle Scale (SPS) LES closure [33]. This formulation effectively frames the SPH equations within a Large Eddy Simulation (SPH-LES) formalism [34,35], where the contribution of sub-grid scale structures to the momentum balance is explicitly accounted for. In this context, $\boldsymbol{\Gamma}_a$ is implemented as

$$\boldsymbol{\Gamma}_a = \sum_b m_b \frac{4\nu \mathbf{r}_{ab}\cdot\boldsymbol{\nabla}_a W_{ab}}{\left(\rho_a+\rho_b\right)\left(r_{ab}^2+0.01h^2\right)}\boldsymbol{v}_{ab} + \sum_b m_b\left(\frac{\tilde{\tau}_a^{ij}+\tilde{\tau}_b^{ij}}{\rho_a\,\rho_b}\right)\nabla^i W_{ab}, \tag{5}$$

where ν is the kinematic viscosity. The former term is given by the laminar viscosity, whereas the latter refers to the SPS model. The SPS stress tensor, $\tilde{\tau}^{ij}$, in Einstein notation in coordinate directions i and j, is defined according to SPS strain tensor $\tilde{S}^{ij}$ as follows

$$\tilde{S}^{ij} = -\frac{1}{2}\left(\frac{\partial \tilde{v}_i}{\partial x_j}+\frac{\partial \tilde{v}_j}{\partial x_i}\right), \tag{6}$$

being $\tilde{\mathbf{v}}$ the filtered velocity vector and $\mathbf{x}$ the position vector of the particle. Adopting the canonical Smagorinsky model, originally adapted for Lagrangian methods by Gotoh et al. [36], the eddy viscosity is modelled as

$$\frac{\tilde{\tau}^{ij}}{\rho} = \nu_t\left(2\tilde{S}^{ii}-\frac{2}{3}\tilde{S}^{ii}\delta^{ij}\right)-\frac{2}{3}C_L d_p^2\delta^{ij}|\tilde{S}^{ij}|^2, \tag{7}$$

where $\nu_t = \left(C_S d_p\right)^2|\tilde{S}^{ij}|^2$ is the eddy viscosity, $C_S = 0.12$ is the Smagorinsky constant, $C_L = 0.0066$, $|\tilde{S}^{ij}| = \frac{1}{2}\left(\tilde{S}^{ij}\tilde{S}^{ij}\right)^{1/2}$ is the local strain rate, and δ^{ij} represents the Kronecker delta function.

While it is acknowledged that dynamic sub-grid scale models offer superior local adaptivity for complex flows (e.g., [37]), the constant-coefficient SPH-LES approach remains a well-established and stable standard for hydraulic applications involving complex 3D boundary interactions. In the present study, this closure ensures the numerical stability required to achieve a statistically steady hydrodynamic state over complex scoured topographies, providing a physically consistent description of the macroscopic propeller-induced flows.

In this work, the above two formulations to model the dissipation term $\boldsymbol{\Gamma}_a$ will be tested in the numerical simulations.

Owing to the use of a weakly compressible SPH formulation, the following equation of state to determine p from ρ is adopted

$$p = \frac{c_s^2\rho_0}{\gamma_p}\left[\left(\frac{\rho}{\rho_0}\right)^{\gamma_p}-1\right], \tag{8}$$

being ρ_0 the initial density at the free surface and $\gamma_p = 7$ the water polytropic index.

To prevent unacceptable anisotropic distributions of the particles, which may create voids within the fluid and the appearance of noise in the velocity and pressure field for relevant fluid-solid interactions, a Fickian-based PST is applied [38,39]. Following the implementation described in Domínguez et al. [22], the shifting displacement $\delta\mathbf{r}_a$ is computed as

$$\delta\mathbf{r}_a = -A_s h\|\mathbf{v}_a\|\nabla C_a \Delta t, \tag{9}$$

where A_s is a dimensionless shifting magnitude, $\|\mathbf{v}_a\|$ is the target velocity magnitude, and Δt is the time step. The term ∇C_a represents the gradient of the particle concentration, which is calculated through the kernel operator as

$$\nabla C_a = \sum_b \frac{m_b}{\rho_b}\nabla_a W_{ab}. \tag{10}$$

To ensure a stable and regular particle distribution throughout the simulations, the dimensionless coefficient was set to A_s = 2.0. In the current single-phase modelling approach, the shifting displacement is deactivated for particles located at or near the free surface. This is achieved by evaluating the divergence of the position vector $\nabla\cdot\mathbf{r}_a$

$$\nabla\cdot\mathbf{r}_a = \sum_b \frac{m_b}{\rho_b}\mathbf{r}_{ab}\cdot\nabla_a W_{ab}. \tag{11}$$

A particle is identified as belonging to the free surface if $\nabla\cdot\mathbf{r}_a$ is less than a specific threshold. For the present 3D simulations, a free-surface detection threshold of 2.75 was employed. This specific value ensures that the shifting remains active strictly within the bulk of the fluid domain, thereby preserving the integrity of the free surface throughout the jet development.

2.2. Boundary conditions

In this study, the solid boundaries were treated using the modified Dynamic Boundary Conditions (mDBCs) [40]. Unlike standard Dynamic Boundary Conditions [41], mDBCs treat boundary particles as part of a continuum fluid layer. This approach eliminates the non-physical density discontinuities that commonly arise at solid interfaces, yielding smoother pressure fields and improving stability in strongly sheared regions such as the scoured bed. In the present modelling, all solid boundaries were assigned no-slip conditions to ensure that the fluid velocity matches that of the adjacent solid surfaces. No special boundary treatment for near-wall turbulence modelling, such as wall functions or the enforcement of a logarithmic law, was implemented in the current setup. The SPS turbulence model and the artificial viscosity term were applied uniformly throughout the fluid domain, assuming that the interaction between fluid and boundary particles follows the standard SPH formalism without analytical corrections to the velocity

profile in the viscous sublayer. Fluid-solid interactions at the boundaries were exclusively handled through the standard mDBCs, consistent with the adopted SPH solver. While this approach guarantees robust fluid–structure interaction, the absence of dedicated near-wall turbulence models may contribute to a conservative estimation of turbulence production in the immediate vicinity of the solid interfaces.

To reproduce the steady flow of the laboratory experiment related to the presence of a background current, specific boundary conditions were assigned at both the inlet and outlet of the channel. A buffer-layer algorithm was adopted to discretise the boundaries, allowing the prescription of flow variables and the continuous generation or removal of particles [42]. At the inlet, the bulk velocity and particle refilling beneath the target water depth were imposed, whereas the outlet employed an extrapolation-based approach from particles of the domain to maintain numerical stability and avoid undesired flow reflections.

To simulate the case involving surface regular waves, a movable solid boundary was used to reproduce a piston paddle wave maker [43]. The modelling of these waves was carried out by applying a second-order wave maker theory to avoid the occurrence of unwanted secondary waves [44]. To avoid undesired impulsive phenomena in the numerical wave channel, which could perturb the flow field, the time law of horizontal displacement of the piston-type wavemaker is initially modified by a ramp function. An active absorption system was also used to avoid re-reflected waves, as well as a passive absorption system at the end of the flume [43].

2.3. Nesting strategy

The hydrodynamics of marine propellers involve sub-millimetre geometric scales that require extremely fine particle resolutions to accurately resolve blade-induced vortices. Indeed, the used blade thickness of propellers in laboratory experiments, as in the present cases, is approximately 1 mm, necessitating a particle spacing ensuring a minimum number of particle layers across the thickness, so that the adopted kernel support radius is fully contained within the solid [13]. Although essential for representing the near-field PJ dynamics, such fine resolutions become prohibitively expensive when extended to the entire flume-scale domains.

To overcome this challenge, a two-step SPH nesting methodology was developed. First, a high-resolution simulation was performed in a confined domain surrounding the propeller, where the detailed 3D flow field was sampled over a Recording Mesh (RM). Details of the high-resolution simulation domain can be found in Ferraro et al. [13]. The goal of this step was to resolve the fully turbulent and helical flow structure generated by the propeller blades (see Ferraro et al. [13] for further details). In the present implementation, the RM, used to sample the flow field from the high-resolution propeller-scale simulation, was positioned immediately downstream of the propeller geometry at a distance $x = l_{\mathrm{RM}}$, where x is the streamwise coordinate, with its origin located at the propeller blades plane (see Fig. 1). The RM is represented by a plane located as close as numerically feasible to the blade trailing edge without directly interacting with the solid geometry. This location is selected to ensure that the dominant features of the PJ are already developed and can be accurately sampled, while still being remaining representative of the near-field flow dynamics. The distance is set to $l_{\mathrm{RM}} = 0.5D_p$, where D_p is the propeller diameter. It is emphasised that the RM does not constitute a physical boundary and can be positioned at any suitable downstream location depending on the specific application. The RM consists of a regular, structured grid spanning a rectangular region of width L_y and height L_z, both equal to $1.5D_p$ and centred on the propeller axis. Although the resolution of the RM could, in principle, be selected independently of the recorded particle spacing, for simplicity, the mesh resolution is defined by a uniform spacing ($\Delta_y = \Delta_z$) corresponding to the interparticle distance of the high-resolution simulation. Moreover, the RM sampling frequency was set to 100 Hz. For the propeller rotational speed adopted in the experiments ($n = 700$ rpm), corresponding to a fundamental rotational frequency of approximately 11.7 Hz, this sampling rate provides more than eight samples per revolution. This temporal resolution is therefore sufficient to capture the dominant hydrodynamic features of the propeller-induced jet, including the primary unsteady structures associated with blade passage and jet development [13]. The transfer of information from particles to the RM involves a spatial interpolation process, which inherently introduces an approximation [17]. It is worth noting that while the RM is defined as a 2D transverse plane, it captures the full 3D velocity components (u, v, and w) at each grid node. This ensures that the essential three-dimensional characteristics of the propeller jet, specifically its axial momentum, swirl, and radial expansion, are faithfully preserved and subsequently projected into the larger nested domain. Although this offline one-way nesting approach introduces a spatial simplification that inherently filters the finest turbulent eddies, it effectively captures the macroscopic momentum transfer and the periodic wake structures that drive the hydrodynamic patterns over the complex bathymetry. The physical consistency of this approximation is further supported by the overall agreement with both experimental data and numerical simulations presented in Section 4.

Next, the RM containing the sampled three-dimensional flow field was mapped into the large-scale domain, where it effectively acts as a Nesting Mesh (NM) embedded within a Relaxation Zone (RZ), enabling the transfer of the recorded flow field to the coarse-resolution simulation. The NM is defined as a plane whose resolution corresponds to that adopted for the RM in the high-resolution simulation. Therefore, the NM spacing matches the grid used to sample the velocity field from the propeller-resolved domain and is therefore independent of the particle resolution adopted in the outer coarse-scale simulation. The NM is concentrically aligned with the propeller's rotational axis to ensure consistent transfer of the velocity field. In this work, the outer domain was intentionally discretised using a coarse spatial resolution ($d_p = 5$ mm), in order to keep the overall computational cost within feasible limits when simulating a multi-metre-scale scoured bathymetry.

The transfer of flow information between the two simulations follows the conceptual framework of the MESH-IN technique [17]. However, a key distinction is introduced in the present approach: rather than prescribing the pre-recorded flow field at the inlet boundary of the coarser simulation, this information is directly imposed within a localised fluid region corresponding to the area most strongly affected by the propeller-induced jet.

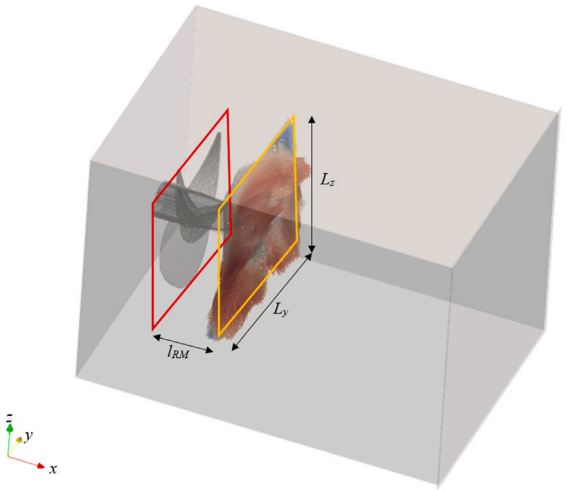

Fig. 1. Representation of the high-resolution simulation domain with propeller geometry and the RM position. The red square represents the blade plane, whereas the orange square is the RM plane.

The spatial configuration of the RZ and NM adopted in the nesting procedure is illustrated in Fig. 2. The figure shows complementary views of their position within the computational domain and their geometric relationship with the characteristic domain dimensions. Specifically, panel (a) shows an axonometric view of the position of the RZ, while panel (b) presents an enlarged view including the propeller for illustrative purposes only. Panels (c) and (d) highlight, respectively, the transverse dimensions of the NM domain, within which a damping border region of thickness δ_{RZ} is included, and the lateral position of the NM centred along the streamwise RZ length L_x. The size of δ_{RZ} is defined below. In this study, the NM dimensions L_y and L_z were set equal to those of the RM.

The transition between the imposed and freely evolving flow is controlled by a border damping layer of thickness δ_{RZ} (introduced earlier), applied at the relaxation-zone boundaries, whose value depends on the specific case. This damping layer enforces a smooth velocity transition and effectively suppresses spurious reflections at the interface between forced and unforced regions. An example of the damping function F_{DMP} applied along the y-axis is presented in Fig. 2e. The relaxation strength within the RZ increases up to the NM location and subsequently decreases toward the end of the RZ, allowing the imposed flow to progressively transition to the dynamics of the larger-scale domain. Specifically, the spatial distribution of the weighting function F_{RZ} within the RZ follows a hyperbolic profile (see Fig. 2f). This function is governed by the parameter $\beta = 3$, which controls the steepness of the transition between the core region, where the imposed flow field is dominant, and the outer damping layer. This choice ensures a sufficiently sharp yet numerically stable blending of velocities. The maximum strength of the weighting function is prescribed through $\psi = 0.9$, which strongly drives particle velocities toward the target mesh-based velocity field within the core of the relaxation zone while retaining limited local flow adaptability. These settings ensure that the RZ length remains minimal and comparable to the characteristic dimensions of the propeller geometry. The temporal enforcement of the imposed velocity field is scaled relative to the SPH time step by a multiplicative coefficient $Cdt = 1000$. This scaling accelerates convergence toward the target velocity field without introducing numerical stiffness, ensuring consistent momentum injection throughout the simulation (for further details, see [21]).

In summary, this configuration allows particles to be smoothly accommodated by the imposed flow field in the upstream region, while allowing for a gradual transition to freely evolving particle motion downstream. Such a mesh design ensures numerical stability of particle transport across the mesh interfaces and stable injection of momentum into the larger domain, in accordance with the approach proposed by Altomare et al. [21]. Building upon these foundations, the specific implementation developed here introduces a key methodological shift from a global boundary-based coupling to a localised internal nesting. By repurposing RZ for inter-domain momentum transfer rather than simple wave damping, and synchronising them with a periodic embedding of the 3D velocity signature, the model effectively captures the complex helical wake and blade-passage effects. This integrated framework not only maintains manageable computational costs but also provides a robust tool for the systematic study of propeller-induced flow interacting with complex 3D scoured topographies under diverse ambient conditions.

3. Experimental set-ups and measurement procedures

Experiments were conducted at two independent hydraulic laboratories to investigate propeller-induced scour under different hydrodynamic conditions. Experiments under still water conditions and with steady open-channel flow were carried out in the *Laboratorio "Grandi Modelli Idraulici"* at the University of Calabria (Italy), while complementary experiments in the presence of waves were performed at the *Laboratorio di Idraulica ambientale e marittima* (LIam) of the University of L'Aquila (Italy). The multi-facility

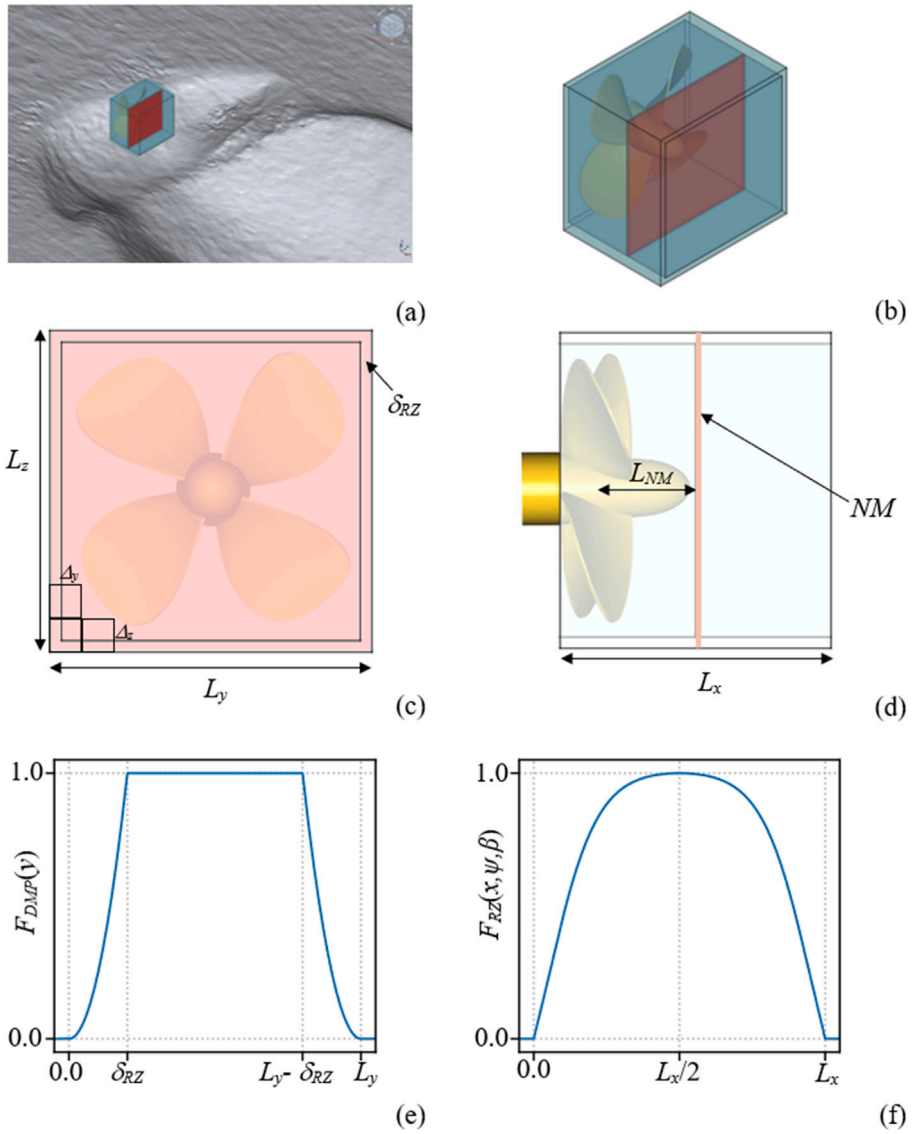

Fig. 2. Spatial configuration of the NM and RZ. (a) Axonometric view showing the position of the RZ within a computational domain. (b) Enlarged view of the RZ, where the propeller is included for illustrative purposes to indicate its relative location with respect to the RZ. (c) Downstream-to-upstream view highlighting the transverse extent of the RZ and the damping border layer. (d) Lateral view showing the position of the NM centred along the streamwise RZ length L_x. (e) Damping function applied to the boundary regions of the y–z plane, with thickness δ_{RZ}. (f) Weighting function along the streamwise RZ length L_x.

experimental dataset was assembled by selecting the most relevant and well-documented experiments from previous publications (see, for more details, [5,14]). This dataset was used to support both direct model validation and qualitative comparison with published results.

The experiments conducted at the University of Calabria employed a recirculating open-channel flume with a rectangular cross-section, 18 m in length and 0.985 m in width, equipped with an upstream flow-conditioning system consisting of a stilling basin, a diffuser, a fine grid, and a honeycomb to dissipate residual turbulence generated by the pump system. Flow discharge was monitored using a calibrated Bazin weir, providing an accuracy within 2%. A recessed test section was installed downstream of the inlet and filled with uniform fine sand characterised by a median grain diameter $d_{50} = 0.69$ mm and a sediment density $\rho_s = 2660$ kg m^{-3}. The propulsion system comprised an electric motor and transmission unit driving a four-bladed, right-handed propeller with a diameter $D_p = 60$ mm, rigidly mounted at the channel centreline. The propeller rotational speed was fixed at $n = 700$ rpm, corresponding to a thrust coefficient $C_t = 0.5$ [45,46]. The propulsion system consisted of a low-voltage inverter, a water-cooling unit, an electric motor, and a transmission system driving the propeller. The propeller rotated clockwise when viewed from downstream and was rigidly mounted on an aluminium frame positioned at the centre of the flume to prevent unwanted vibrations or displacements.

Velocity measurements were performed only for experiments with steady currents, using a four-beam, down-looking Acoustic Doppler Velocimeter (ADV, Nortek Vectrino), following the acquisition and post-processing procedure described in Ferraro et al. [5]. The instrument was configured to measure the three instantaneous velocity components in the streamwise (u), spanwise (v), and vertical (w) directions at discrete locations downstream of the propeller.

Data were acquired at a sampling frequency of 100 Hz over a total recording duration of 600 s at each measurement point, ensuring statistical convergence of first- and second-order velocity moments. The ADV sampling volume was positioned sufficiently above the bed to avoid signal contamination from bed interference, while remaining within the region of interest of the propeller-induced flow. Raw velocity time series were subjected to standard quality-control procedures before statistical analysis. Spurious data points associated with low signal correlation or low signal-to-noise ratio were identified and removed based on threshold criteria, following the methodology adopted by Ferraro et al. [5]. The remaining data were despiked using a phase-space or acceleration-based filtering technique [47] to eliminate impulsive noise without altering the physical content of the signal. After filtering, the velocity time series were used to compute time-averaged velocity components. All statistical quantities were calculated using the effective sampling duration after data rejection, ensuring consistency across measurement locations and experimental conditions.

In contrast, the remaining experimental configurations, including still water and wave-dominated conditions, were not instrumented for velocity measurements. These cases are therefore used to assess the numerical model performance through comparison with established trends and scouring characteristics reported in the literature, rather than through direct pointwise validation.

The experiments involving wave-induced conditions, carried out at the University of L'Aquila, were performed using a wave flume 45 m long, 1.5 m wide, and 2.0 m high. The flume is equipped with a piston-type wave generator with a maximum stroke of 0.75 m, operating in conjunction with an active wave absorption system based on real-time reflection analysis [48].

A sediment cover layer was installed starting approximately 17 m downstream of the wavemaker rest position and extending to the downstream end of the flume, where a passive wave absorber composed of large natural rocks was located. The sedimented region was connected to the offshore section near the wavemaker by a 9.0 m long concrete ramp with a slope of 1V : 20H. The thickest sediment recess box, with a depth of 0.54 m and a length of 3.08 m, was located approximately 25.5 m from the wavemaker rest position. The test section was positioned about 10 m landward of the inshore end of the concrete ramp. The recess box was filled with uniform, well-sorted (monogranular) fine sand characterised by $d_{50} = 0.18$ mm and a uniformity coefficient $C_u = 1.22$. Free-surface elevations were derived from nine resistive wave gauges arranged into three groups of three sensors, allowing standard reflection analysis following the method of Mansard and Funke [49]. The wave gauges were sampled at a frequency of 100 Hz.

In all types of experiments, following established laboratory practice, the temporal evolution of bed changes was monitored until the attainment of a Quasi-Equilibrium Scour (QES) condition (e.g., [5]). QES was identified as the stage at which the scour depth reached a stable value, preceding the complete stabilisation of the scour hole planimetric dimensions. Scour evolution was tracked through repeated bathymetric surveys performed during the experimental runs. At the end of each run, the channel was slowly drained through the bottom outlets to minimise bed disturbance. The final bed morphology was acquired using a photogrammetric survey and processed to reconstruct the three-dimensional scoured bathymetry as a Digital Elevation Model (DEM). The resulting DEMs, shown in Fig. 3 for all the examined cases, were used to define the fixed-bed boundary condition for the numerical simulations.

4. Results

The numerical results presented in this Section are intentionally restricted to a selected set of model configurations. This choice reflects the primary objective of the present work, namely, the development and assessment of a nesting strategy for coupling high-resolution propeller-induced flow fields with laboratory-scale domains.

The spatial resolution adopted in the following simulations corresponds to the coarsest discretisation compatible with numerical stability and with simulation times remaining within reasonable limits for the available computational resources. While increasing the resolution would improve the representation of small-scale flow structures, particularly in the vicinity of the propeller, the associated computational cost becomes rapidly prohibitive when extending the domain to laboratory scales.

High-resolution SPH simulations of propeller jets, such as those reported by Ferraro et al. [13], indicate that an adequate resolution of turbulence generated by blade rotation requires particle spacings on the order of a fraction of the minimum blade thickness, so that the kernel radius is not truncated. Although such resolutions enable the explicit capture of fine-scale vortical and helical structures, they result in particle counts that saturate current computational resources. Applying comparable resolutions to the present laboratory-scale configurations, which include the scoured bathymetry, is therefore not computationally viable.

Accordingly, the present study does not aim at resolving blade-scale turbulent structures. Instead, the focus is placed on reproducing the macroscopic behaviour of the propeller jet at laboratory scale, including jet spreading and interaction with the ambient environment and bathymetry. Within this framework, the nesting approach provides a practical means of bridging the scale gap between locally resolved propeller dynamics and the larger experimental domain.

It is acknowledged that techniques based on variable spatial resolution or adaptive particle refinement [18,19] may offer potential improvements for flows dominated by turbulence generated by rotating propeller blades, where the resolutions required to resolve these structures are quite difficult to reproduce with commonly available computational resources. The nesting strategy adopted herein provides a viable balance between physical realism and computational cost. Specifically, it allows the propeller-induced velocity field to be computed once in a dedicated high-resolution simulation and subsequently reused in multiple simulations where the bathymetry or other environmental parameters may vary. This feature significantly enhances computational efficiency, as the propeller flow does not need to be recomputed for each configuration. In addition, the hydrodynamic effect of the propeller is inherently periodic. Therefore, it is sufficient to record the velocity field over a limited time interval, which can then be cyclically

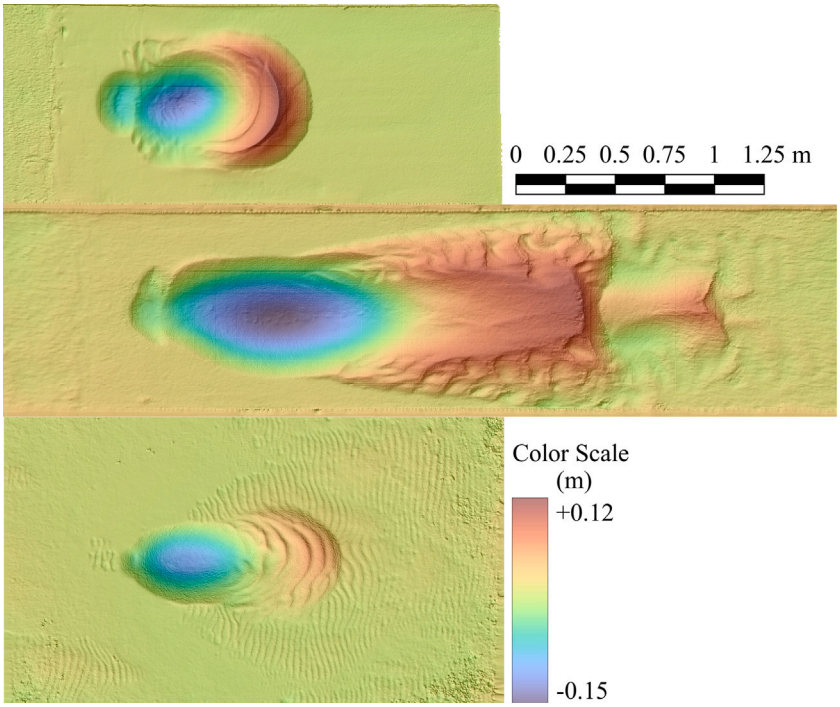

Fig. 3. DEMs under still water conditions (upper panel), steady current conditions (centre panel), and regular wave conditions (bottom panel), showing the bed morphology at the QES stage in each scenario.

imposed in much longer simulations of the outer domain. A fully coupled long-duration simulation resolving the propeller geometry at high resolution within a large-scale domain would remain computationally unfeasible, even when adopting variable spatial resolution techniques. While variable resolution can reduce the total number of particles, it typically increases the computational cost per particle due to the more complex formulation required. Furthermore, the global time step remains constrained by the finest resolution, leading to a substantial increase in the total number of time steps. Consequently, the nesting strategy provides a more practical and computationally efficient alternative for multiscale propeller-driven flow simulations.

Three test cases are reported. The first case regards the interaction between a PJ and an ambient steady current. The numerical results, based on the best balances accuracy, physical consistency, and computational cost, are assessed through comparison with laboratory measurements of the three-dimensional velocity field acquired under current conditions at the QES stage [5]. The validation focuses on velocity profiles extracted downstream of the propeller along x, y, and z directions. For this case, two different dissipative closures implemented in DualSPHysics are considered: (i) the Laminar+SPS turbulence model based on the Smagorinsky formulation [33], and (ii) the standard artificial viscosity approach [32]. The velocity field imposed in the larger-scale SPH domain is obtained through the nesting strategy described in Section 2.3. Then, the same nesting approach has also been applied to a still water configuration and to the presence of surrounding regular waves, following the experimental set-ups at the QES stage adopted by Ferraro et al. [5,14]. Owing to the lack of velocity measurements for comparison purposes, as highlighted in Section 3, attention is therefore focused on the description of the simulated flow field and on the capability of the adopted framework to reproduce the dominant hydrodynamic features of the propeller jet at the laboratory scale. The computational strategies adopted for these numerical cases, including the boundary conditions and the nesting methodology, are identical to those used in the model–experiment comparison of the first test case, thereby ensuring consistency between validation and flow-field analysis. SPH simulations are carried out using the dissipative closure term, which provides a better agreement with laboratory data of the test case with the ambient current.

4.1. Rotating propeller in the presence of a current

4.1.1. Numerical set-up

The numerical domain reproduces the full experimental facility and incorporates the QES bathymetry as a fixed solid boundary. The computational layout, including domain dimensions, boundary conditions, and propeller location, is shown schematically in Fig. 4. The inlet and outlet boundaries impose the ambient current-reproducing laboratory conditions in terms of water depth and discharge, while solid boundaries are applied at the channel bed and sidewalls. The streamwise length of the domain is $L_1 = 64D_p$, the channel width is $B = 16D_p$, and the water depth at the inlet boundary is $h_w = 6D_p$. The propeller axis is positioned at a distance of $6.5D_p$ downstream of the inlet boundary, ensuring a sufficient development length for the imposed current before its interaction

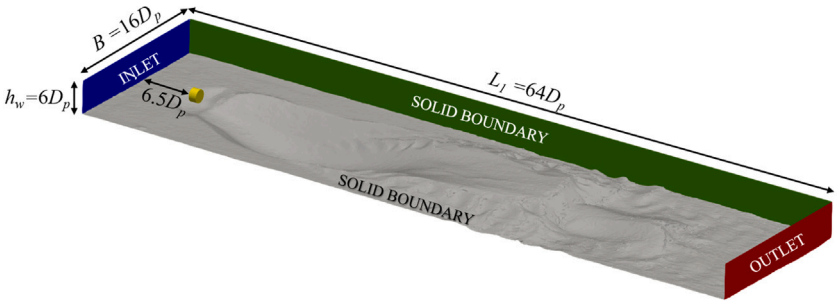

Fig. 4. Computational domain and boundary condition details of the simulation in the presence of an upstream flow.

with the PJ. Within this region, the velocity field sampled from the high-resolution propeller-scale simulation is imposed via the NM along the streamwise direction. The relaxation region is defined as a rectangular box with a streamwise length $L_x = 0.83D_p$ and spanwise and vertical extents $L_y = L_z = 1.0D_p$, centred on the propeller axis. A border damping layer of thickness $\delta_{\mathrm{RZ}} \approx 0.3D_p$ is applied at the relaxation-zone boundaries to ensure a smooth transition between the imposed flow and the freely evolving flow.

4.1.2. Analysis of the velocity field

The first analysis concerns the consistency of SPH results when compared to the experimental data in terms of the streamwise, spanwise, and vertical velocity components along the x, y, and z directions, respectively. In the numerical simulations, velocity data were sampled at fixed spatial locations using a dedicated post-processing measurement tool, which records the three velocity components following an Eulerian approach analogous to point-based ADV measurements. The sampling frequency of the SPH velocity signals was set to 100 Hz, matching the ADV sampling frequency. The SPH velocity time series were not subjected to additional despiking or filtering. To ensure a consistent treatment of experimental and numerical data, both datasets were analysed in terms of temporally averaged velocity components, computed over equivalent averaging intervals.

An initial comparison between numerical predictions and experimental measurements of the velocity field is shown in Fig. 5 along the dimensionless streamwise coordinate x/D_p. The profiles were extracted along the propeller centreline, where the influence of the propeller-induced jet remains significant while progressively interacting with the background current. The streamwise-averaged velocity component, $\overline{u}$, exhibits a gradual decay downstream of the propeller, reflecting the combined effects of jet spreading and turbulent momentum redistribution. The SPH results obtained with the laminar+SPS turbulence model reproduce the overall trend of the measured profiles, capturing both the magnitude and the decay rate of the streamwise velocity with reasonable accuracy. Minor discrepancies are observed in the immediate vicinity of the propeller plane, where velocity measurements are affected by increased scatter and reduced data correlation, as discussed by Ferraro et al. [1]. The spanwise and vertical averaged velocity components, $\overline{v}$ and $\overline{w}$, respectively, display smaller amplitudes and increased variability, consistent with their secondary role in the streamwise development of the PJ. The laminar+SPS model provides a qualitatively consistent representation of these profiles. In contrast, simulations employing artificial viscosity exhibit oscillatory behaviour in disagreement with experimental data, as highlighted in SPH literature when turbulent flows are involved [20,37]. Overall, the comparison along the streamwise direction supports the ability of the SPH model with laminar+SPS closure to represent the macroscopic evolution of the PJ over the laboratory-scale domain.

Fig. 6 presents the three components of the velocity vector measured along the dimensionless spanwise direction, y/D_p, at $z/D_p = 0$, corresponding to the horizontal plane passing through the propeller hub centre. These measures were sampled at a distance from the propeller location of $x/D_p = 4$. The streamwise averaged velocity component ($\overline{u}$) exhibits a jet-like distribution with a maximum close to the jet axis and a gradual decay toward the outer regions. The laminar+SPS model reproduces the overall shape of the experimental profiles and provides a reasonable estimate of the peak velocity and jet spreading, except for a small defect in the velocity at the core jet location ($y/D_p = 0$). Some discrepancies are also observed in the outer regions, which may be associated with the combined effects of turbulent modelling and nesting-induced interpolation, which is challenged by the high-velocity gradient at the jet radial edge. The spanwise ($\overline{v}$) and vertical ($\overline{w}$) averaged velocity components are characterised by smaller magnitudes, as expected. The laminar+SPS formulation captures the sign and general trend of these components, although little differences in magnitude persist, particularly away from the jet core. In contrast, the artificial viscosity model systematically predicts a different velocity profile behaviour as well as smoother profiles with reduced velocity gradients, indicating a tendency toward excessive numerical dissipation.

Fig. 7 shows the three velocity components measured along the vertical (z) direction at $y = 0$, corresponding to the vertical plane passing through the propeller hub centre. The vertical distribution of the averaged streamwise velocity component ($\overline{u}$) reflects the interaction between the propeller jet, the background current, and the scoured bathymetry. The laminar+SPS model provides a qualitatively consistent representation of the velocity gradients and the jet core location, although local deviations are observed near the bed ($z/D_p < 0$). These differences are likely influenced by the limited resolution of the outer domain imposed by computational constraints. Finally, the vertical ($\overline{w}$) and spanwise ($\overline{v}$) averaged velocity components exhibit relatively small amplitudes and display narrow scatter in the experimental data. The laminar+SPS model reproduces the general structure of these profiles, whereas

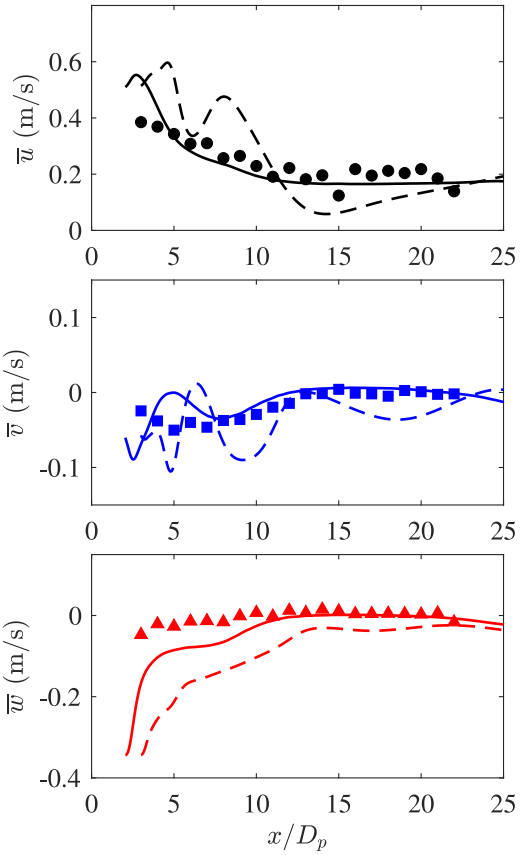

Fig. 5. Streamwise (top panel), spanwise (middle panel), and vertical (bottom panel) averaged velocity components measured along the dimensionless streamwise direction. Markers denote experimental data, solid lines represent SPH results obtained with the laminar+SPS model, and dashed lines correspond to simulations using artificial viscosity.

the artificial viscosity approach tends to damp secondary motions, leading to a reduced representation of vertical and spanwise momentum exchange.

To highlight the macroscopic description of the PJ flow field, consistent with the objectives of the present study, the numerical simulation of the velocity magnitude field obtained with the laminar+SPS model is shown in Fig. 8. The instantaneous velocity fields are visualised directly from the SPH particle velocities. Consequently, the plotted fields retain the intrinsic particle-scale variability typical of Lagrangian SPH representations. No additional spatial filtering or remapping onto a fixed Eulerian mesh was applied in order to preserve the native Lagrangian structure of the SPH solution and avoid the introduction of interpolation-induced smoothing.

The flow field visible in the vertical slide is characterised by a well-defined jet core emerging from the mesh location and propagating downstream under the combined effects of ambient current (Fig. 8a). In the immediate vicinity of the propeller, the velocity field is dominated by a concentrated region of high rotating momentum, as visible in Fig. 8b, while spanwise and vertical velocity components remain comparatively weaker in the outer region than in the jet core. Specifically, following Ferraro et al. [5], an initial confinement region of the jet is observed. Here, a double-peaked velocity profile with a deflected core is visible in Fig. 8b, which merges into a single peak velocity distribution marking out the established flow zone (Fig. 8c), where a jet spreading appears. Once again, in accordance with Ferraro et al. [5], at elevations higher than the propeller, recirculation induced by velocity gradients between the propeller-induced flow and the ambient free stream promotes a fan-like opening of the jet cone. Further downstream, the jet exhibits progressive lateral (and vertical) spreading deflection caused by the redistribution of momentum. The streamwise velocity decays gradually with distance from the propeller, while radial motions become increasingly relevant, indicating enhanced mixing between the jet and the ambient flow.

The SPH results show a smooth transition between the region directly influenced by the nested velocity field and the far-field flow governed primarily by the imposed current. No spurious reflections or numerical artefacts are observed at the interface between these regions, suggesting that the relaxation-based velocity imposition provides a dynamically consistent coupling between scales.

An analysis of the Sub-Particle Scale Turbulent Kinetic Energy (k_{SPS}) profiles (not shown here) reveals that while the SPH model successfully captures the spatial trends and peak locations associated with the propeller jet expansion, it tends to underestimate the TKE magnitude compared to experimental measurements. This discrepancy is primarily attributed to the relatively coarse spatial

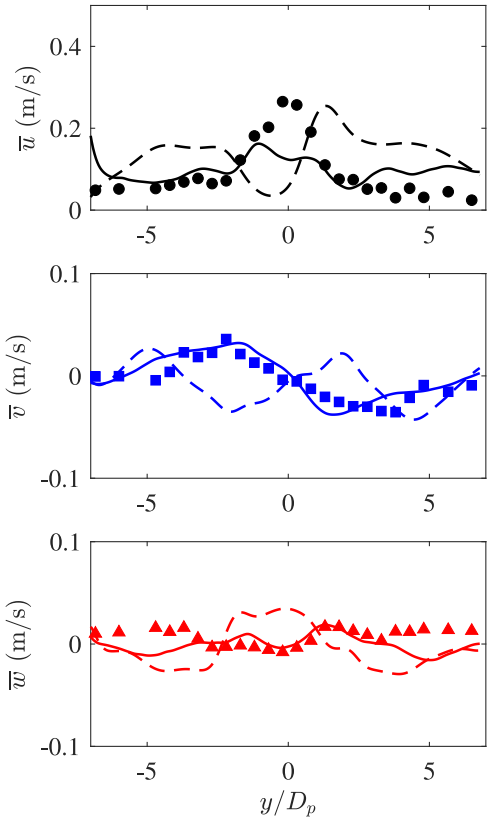

Fig. 6. Streamwise (top panel), spanwise (middle panel), and vertical (bottom panel) velocity components measured along the dimensionless spanwise direction. Markers denote experimental data, solid lines represent SPH results obtained with the laminar+SPS model, and dashed lines correspond to simulations using artificial viscosity.

resolution adopted due to overall computational constraints. This resolution filters out a significant portion of the turbulent scales, thereby increasing the dissipative effect of the standard SPS model in high-shear regions.

It is reiterated that the present simulations are not intended to resolve blade-induced turbulent structures or small-scale vortical dynamics, which would require resolutions comparable to those adopted in fully blade-resolved studies (e.g., [13]). Instead, the objective is to reproduce the dominant flow features governing PJ development at the laboratory scale. Within this framework, the nesting strategy emerges as an effective and computationally feasible approach for studying propeller-driven flows in extended domains in the present case.

4.1.3. Validation model discussion

Overall, the previous comparison of velocity profiles indicates that the laminar+SPS turbulence model provides a more physically consistent description of the propeller jet hydrodynamics than the artificial-viscosity formulation. The Smagorinsky sub-particle closure model appears better suited to representing turbulent mixing and jet spreading, particularly in regions characterised by strong velocity gradients, according to Ferraro et al. [13].

Nevertheless, the agreement between numerical and experimental results should be interpreted in light of the modelling assumptions adopted in this study. The nesting strategy introduces interpolation-related approximations (Section 2.3), whereas boundary conditions and roughness effects are parameterised via mDBCs and an effective-viscosity scaling (Section 2.2). Despite these limitations, the SPH model with laminar+SPS closure reproduces the main features of the measured velocity field, supporting its applicability for simulating propeller jet flows over scoured bathymetries under current conditions.

To assess the differences between experimental and SPH velocity fields obtained using the two adopted dissipation terms, two metrics are employed. The metrics are applied to the averaged velocity fields $\overline{\mathbf{u}}$, obtained from the averaged streamwise $\overline{u}$, spanwise $\overline{v}$, and vertical $\overline{w}$ components along the x, y, and z directions, respectively. Local indices are first computed at each spatial location along all directions. Subsequently, global indices are obtained by spatially averaging the local values, yielding single metrics that quantify the overall agreement between experimental and numerical velocity vectors.

The first metric is the Relevance Index, RI, which enables a quantitative comparison between two vector fields by capturing differences in vector orientation and thus providing a measure of their directional agreement. This index has been widely applied to

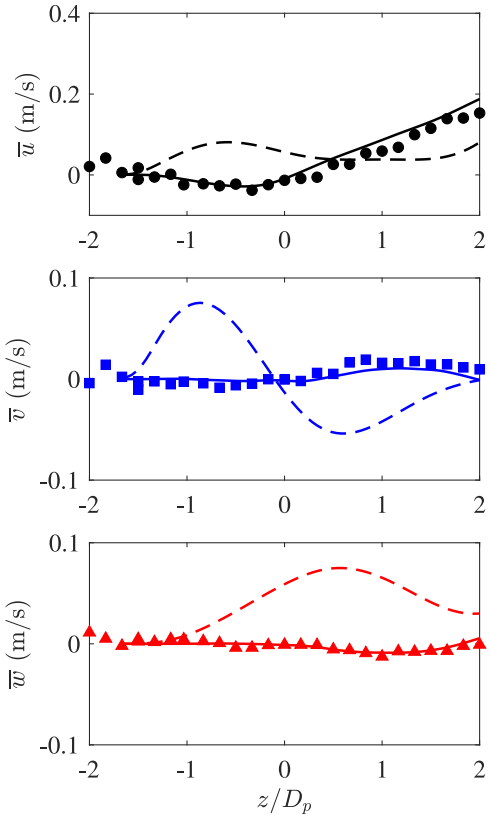

Fig. 7. Streamwise (top panel), spanwise (middle panel), and vertical (bottom panel) averaged velocity components measured along the dimensionless vertical direction. Markers denote experimental data, solid lines represent SPH results obtained with the laminar+SPS model, and dashed lines correspond to simulations using artificial viscosity.

validate numerical simulations in engine and turbulent flow studies (e.g., [50,51]). The RI, introduced by Liu and Haworth [52], is calculated as

$$RI = \frac{1}{N}\sum_{i=1}^{N}\frac{\overline{\mathbf{u}}_i^{\text{exp}}\cdot\overline{\mathbf{u}}_i^{\text{SPH}}}{\left\|\overline{\mathbf{u}}_i^{\text{exp}}\right\|\left\|\overline{\mathbf{u}}_i^{\text{SPH}}\right\|}, \tag{12}$$

where N is the total number of sampling points along each direction, $\|\cdot\|$ denotes the Euclidean norm of the vector, and the superscripts exp and SPH refer to the experimental and SPH results, respectively. Specifically, the SPH data were obtained using either the laminar+SPS LES closure or the artificial viscosity as the dissipation model. The RI ranges between −1 and 1, with values of 1 indicating perfect agreement between experimental and numerical velocity vectors.

The second metric employed is the Magnitude Index, MI, which measures the similarity between the magnitudes of corresponding velocity vectors, independently of their direction [53]. As in the case of the RI, its application was largely diffused to validate numerical results for various flow conditions (e.g., [51,54]). The MI is determined as

$$MI = \frac{1}{N}\sum_{i=1}^{N}1-\frac{\|\overline{\mathbf{u}}_i^{\text{exp}}-\overline{\mathbf{u}}_i^{\text{SPH}}\|}{\|\overline{\mathbf{u}}_i^{\text{exp}}\|+\|\overline{\mathbf{u}}_i^{\text{SPH}}\|}. \tag{13}$$

The MI gives values oscillating between 0 and 1, with greater values corresponding to a better agreement between numerical and experimental data.

Fig. 9 shows the values of RI and MI computed for the mean experimental and numerical velocity vector $\overline{\mathbf{u}}$, which was subsequently spatially averaged along the x, y, and z directions. For all cases, higher RI and MI values are associated with the use of the laminar viscosity+SPS turbulence model, rather than the application of the artificial viscosity, confirming that the former dissipation approach provides a better matching with the laboratory data. This difference is particularly pronounced along the z direction. However, an overall better agreement between experimental and numerical results (i.e., indices close to 1) is observed along the x and y directions, especially for RI. This indicates that the numerical results are more consistent with the experimental data in terms of velocity vector orientation than in terms of velocity magnitude.

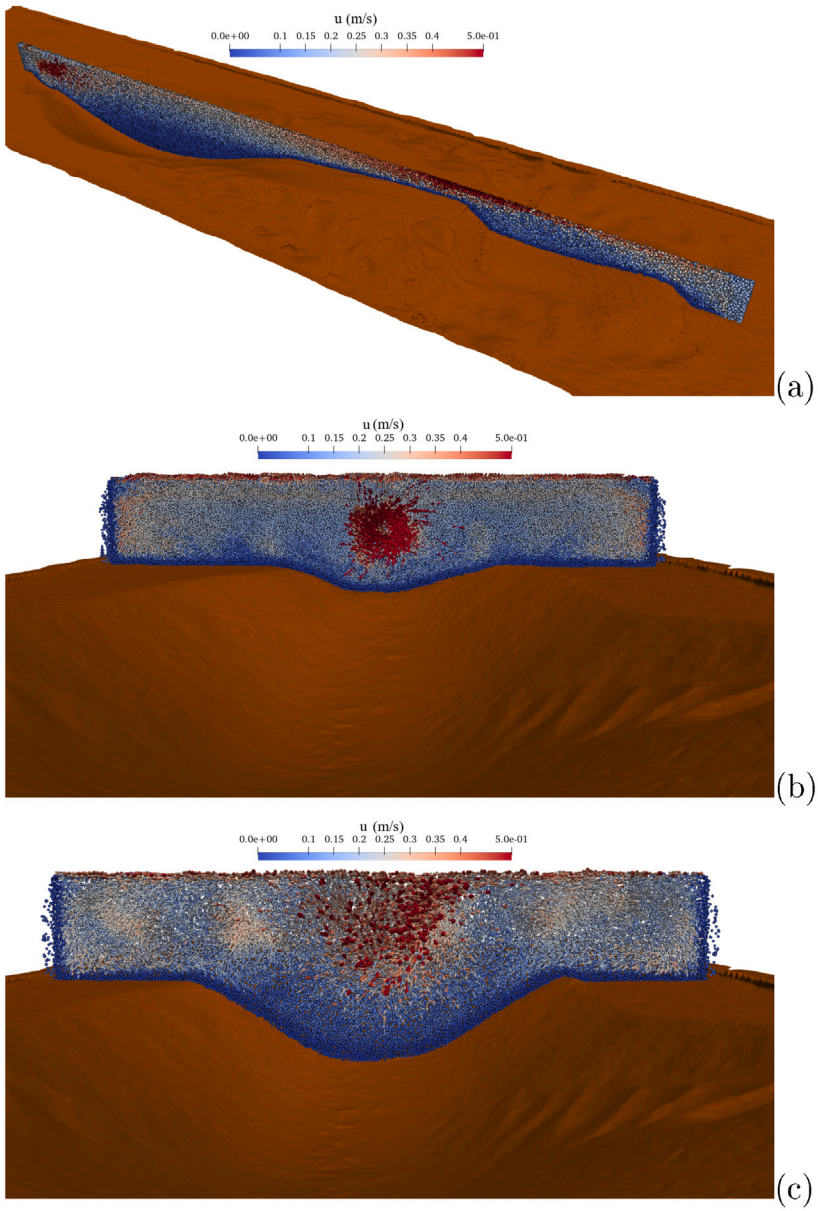

Fig. 8. Numerical simulation of the velocity magnitude field in the presence of a channel flow. (a) vertical cutting plane at the propeller centre location ($y/D_p = 0$); (b) spanwise cutting plane at $x/D_p = 1$; (c) spanwise cutting plane at the maximum scour hole location.

4.2. Rotating propeller in still water conditions

This Section presents a second application of the nesting strategy of a rotating propeller, operating in this case under still water conditions. The purpose of this numerical analysis is to demonstrate the applicability of the proposed SPH nesting strategy to a canonical configuration and to provide insight into the resulting flow field in the absence of an ambient current.

The numerical resolution and the nesting methodology are identical to those adopted for the channel-flow case. In particular, the velocity field generated by a high-resolution propeller-scale simulation is embedded into a larger, coarse-resolution SPH domain through the same relaxation-based approach described in Section 2.3. This ensures consistency across configurations and allows the effect of the surrounding fluid to be isolated. Based on the SPH results obtained through two different dissipative closure terms for the test case with the ambient current (see Section 4.1), the present simulation is carried out by the Laminar+SPS turbulence model.

In particular, the still water simulation is performed within a three-dimensional computational domain that is set to ensure sufficient clearance between the propeller location and the domain boundaries in all directions (see Fig. 10). Thereby, it is guaranteed

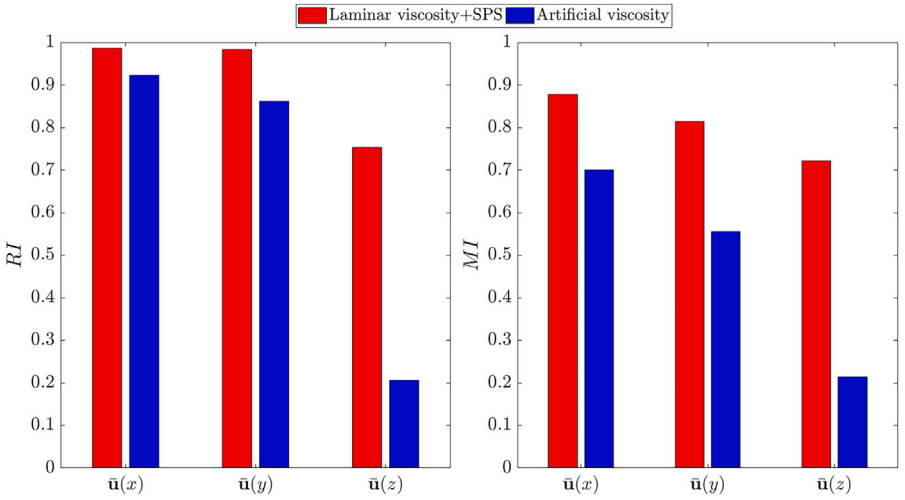

Fig. 9. (a) Relevance Index (RI) (left panel) and Magnitude Index (MI) (right panel) computed for the averaged velocity vector $\bar{\mathbf{u}}$ and subsequently spatially averaged along the x, y, and z directions.

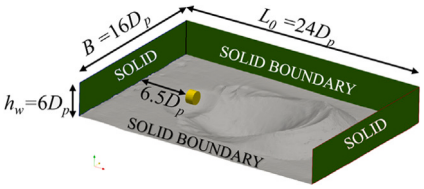

Fig. 10. Computational domain and boundary condition details of the simulation in still water conditions.

that the jet will evolve without artificial confinement. The solid boundaries are enforced at a scoured bathymetry at the QES stage following the experimental results by Ferraro et al. [5], as well as at all lateral boundaries of the computational domain. Unlike the case with the background current, the streamwise length is reduced and equal to $L_0 = 24D_p$ because of the smaller influence of PJ in modifying the mobile bed at the QES stage, whereas channel width, water depth, and propeller position from the inlet boundary remain unchanged. The flow motion within the domain is then generated solely by the propeller-induced momentum introduced through the nested velocity field, with no externally imposed background current. This setup provides a controlled framework for analysing the intrinsic characteristics of the PJ under quiescent surrounding conditions. The velocity field sampled from the high-resolution propeller-scale simulation is imposed within the relaxation zone along the streamwise direction. The relaxation region is defined as a rectangular box of streamwise length $L_x = 0.83D_p$ and spanwise and vertical extents $L_y = L_z = 1.0D_p$, centred on the propeller axis. A damping layer of thickness $\delta_{\mathrm{RZ}} \approx 0.3D_p$ is applied at the boundaries of the relaxation region to ensure a smooth transition between the imposed flow and the freely evolving SPH solution.

The longitudinal structure of the velocity magnitude field is examined on a vertical plane aligned with the propeller axis and passing through its geometric centre, as shown in Fig. 11a. Particles coloured according to the velocity scaled by the local velocity magnitude illustrate the development of the PJ downstream of the propeller. The streamwise velocity field obtained for the still water configuration exhibits the main characteristics commonly associated with propeller jets. To assess the velocity direction, velocity vectors scaled by the local velocity magnitude are superimposed on the velocity contour maps in Fig. 11b and c, highlighting the vortical structure of the flow. Fig. 11b shows that, immediately downstream of the propeller (i.e, $x/D_p = 1$), the flow is characterised by a low-velocity region associated with the propeller hub, followed by the development of a double-peaked velocity profile (Fig. 11c). This feature, which is well documented in experimental and numerical studies of PJs, as reported in the comprehensive review by Wei et al. [3], is captured by the SPH simulation. Further downstream, the wake jet loses its coherence, making it difficult to recognise the single peak typical of the transition from the flow establishment region to the zone of established flow.

The simulated jet displays a progressive radial expansion with increasing distance from the propeller, with an approximately linear growth of the jet width in the near field. This behaviour indicates that confinement effects play a limited role in governing PJ development within this region. Although discrepancies are observed in the detailed distribution of the velocity field, the overall structure and streamwise evolution remain consistent with the behaviour of propeller jets under still water conditions. The observed differences are likely associated with the presence of steep velocity gradients at the radial edge of the jet wake. Such regions are known to pose challenges for SPH-based approaches, particularly in the representation of shear layers separating the jet core from the surrounding quiescent fluid, where strong Kelvin–Helmholtz-type instabilities may develop. A more detailed investigation of this

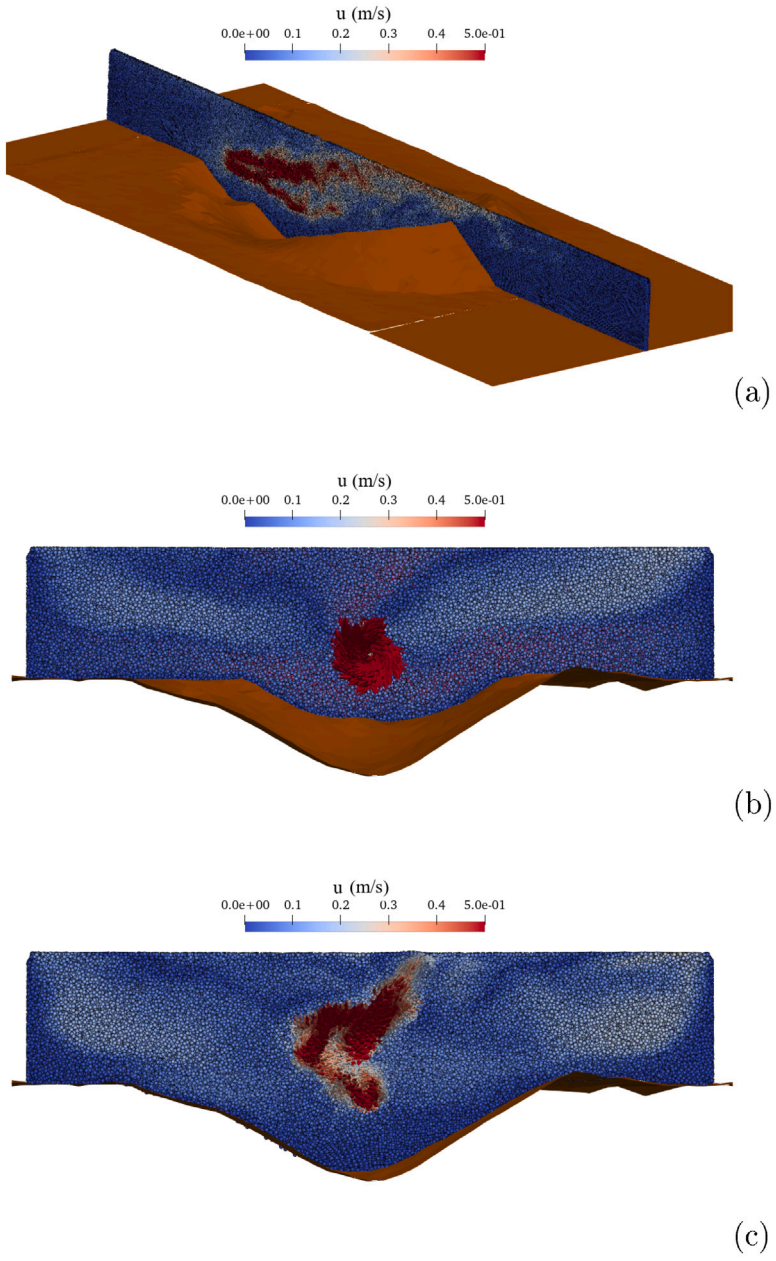

Fig. 11. Numerical simulation of the velocity magnitude field in still water conditions. (a) vertical cutting plane at the propeller centre location ($y/D_p = 0$); (b) spanwise cutting plane at $x/D_p = 1$; (c) spanwise cutting plane at the maximum scour hole location.

regime would require enhanced resolution or alternative turbulence modelling strategies to accurately capture the wake-ambient flow interaction.

It is emphasised that these limitations are intrinsic to the numerical representation of high-shear interfaces and are not related to the nesting strategy introduced in the present work, which remains effective in transferring the propeller-induced momentum to the larger-scale computational domain.

4.3. Rotating propeller in the presence of waves

The third test case regards the interaction between a PJ and regular surface waves. As in the case of still water conditions, the current analysis is performed numerically only to demonstrate the capability of the developed nesting strategy in capturing the main features of this complex hydrodynamic phenomenon. The computational strategies, including the nesting method, are the same as

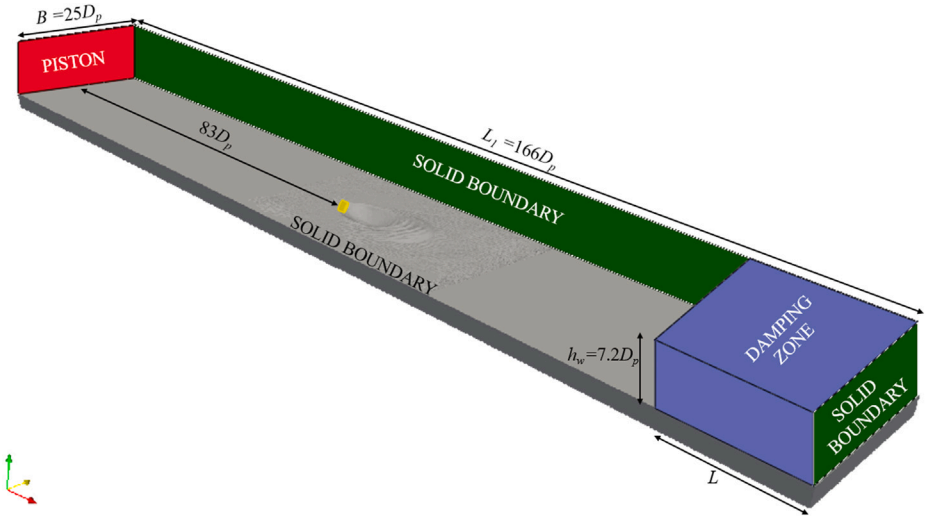

Fig. 12. Computational domain and boundary condition details of the simulation in the presence of regular waves.

those adopted for the previous test cases, as well as the use of the laminar+SPS turbulence model. To limit the computational cost, the adopted numerical domain reproduces only a portion of the experimental layout presented by Ferraro et al. [14]. In particular, the inlet solid boundary corresponds to the cross-section where the laboratory wave gauge closest to the scoured bathymetry was installed. This wave gauge was located 1.7 m upstream of the propeller [14], ensuring a well-defined wave field during its interaction with the PJ, as this distance exceeds the incident wavelength. The experimental wave parameters, namely a wave height of $H = 0.114$ m and a wave period of $T = 1$ s, were used to generate a train of regular waves modelled as third-order Stokes waves. Wave generation was implemented using a piston-type wavemaker, represented numerically by a moving solid boundary. As shown in Fig. 12, the streamwise length of the computational domain is $L_0 = 166D_p$, the channel width is $B = 25D_p$, and the water depth at the inlet boundary is $h_w \approx 7.2D_p$. The propeller-induced velocity field is introduced into the coarse-resolution domain through a relaxation zone centred at $x = x_p$, immediately downstream of the propeller location. In the present configuration, the centre of the relaxation zone is located at $x_p \approx 83D_p$. The relaxation region is defined as a rectangular box with a streamwise length $L_x = 0.83D_p$ and spanwise and vertical extents $L_y = L_z = 1.0D_p$, centred on the propeller axis. Within this region, the velocity field sampled from the high-resolution propeller-scale simulation is imposed along the streamwise direction. A border damping layer of thickness $\delta_{RZ} \approx 0.2D_p$ is applied at the relaxation zone boundaries to ensure a smooth transition between the imposed and the freely evolving flow. The scoured bathymetry corresponding to the QES condition, along with the lateral boundaries and the final wall, is treated as solid boundaries.

In the present numerical wave flume, the duration of the ramp function is set to T to avoid initial transient effects. The downstream portion of the flume is characterised by a damping zone, implemented as a passive wave absorption system, with a length set equal to the incident wavelength ($L = 1.61$ m), as commonly adopted in the SPH literature (e.g., [21]). This strategy allows suppression of wave reflections in the region where the flow field induced by the interaction between the PJ and the wave motion is analysed. The value of L is determined using the linear dispersion relation for third-order Stokes waves [55], as a function of the incident wave period and the local water depth at the position of the wave gauge used to monitor the incoming wave conditions.

Fig. 13 shows the streamwise velocity field simulated by the SPH model and associated velocity vectors in the vertical plane. Four significant time instants related to the wave passage at the propeller location are analysed. Considering a representative wave cycle of the regular motion, they refer to zero up-crossing, crest, zero down-crossing, and trough instants. Paying attention to the zero-up-crossing instant (Fig. 13a), the streamwise velocity field induced by the wave motion is in accordance with that generated by the PJ within an influence area corresponding approximately to the whole scoured bed. This interaction leads to a larger horizontal PJ extension that, in still water conditions and, owing to the high streamwise velocity, a spreading of the jet portion toward the bottom due to the Coandă effect, as noticed in similar contexts by Wei et al. [3] and Ferraro et al. [5]. Concerning the wave crest instant (Fig. 13b), a shortening of the PJ in the scoured zone is notable with respect to the previous instant. This is due to the occurrence of the negative streamwise velocity in a relevant portion of the mentioned area. Furthermore, the velocity change from positive to negative values downstream of the PJ induces a vertical spread of the jet toward the free surface. The analysis of the streamwise velocity field at the zero down-crossing instant in correspondence with the propeller position is characterised by the appearance of a negative trough-induced velocity in the whole scoured area (Fig. 13c). This effect results in a general jet confinement in both the streamwise and vertical directions. In the last time instant investigated and related to the wave trough (Fig. 13d), the PJ is subject to a partial negative horizontal velocity field due to the wave motion. This leads to an initial confinement of the jet, followed by vertical spreading toward the free surface due to its interaction with the positive and negative wave-induced velocities.

Overall, the above numerical findings reproduced by SPH are quite in accordance with the RANSE simulations with the k-ω Shear Stress Transport (SST) turbulence closure model reported in Ferraro et al. [14] under the same wave, propeller, and

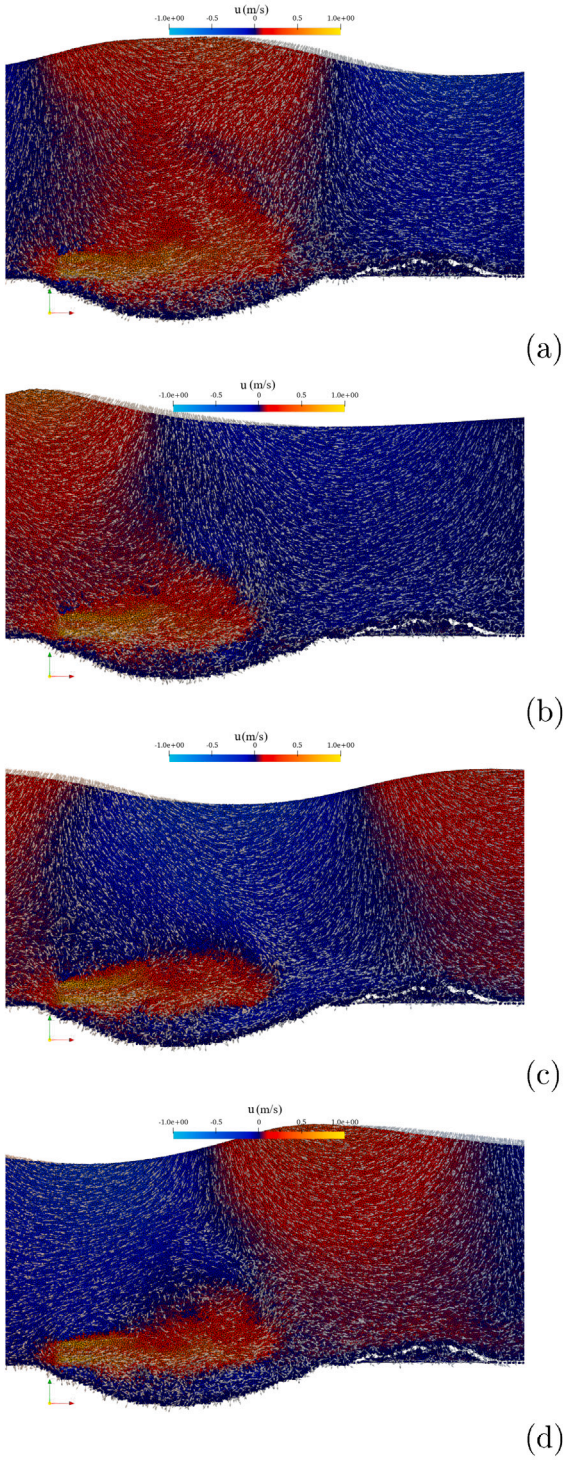

Fig. 13. Numerical streamwise velocity field and associated velocity vectors along the vertical plane in correspondence with the wave passage of four significant instants at the propeller location. (a) zero up-crossing; (b) crest; (c) zero down-crossing; (d) trough.

bathymetry conditions. This confirms that the adopted nesting strategy enables a realistic representation of the main features of this hydrodynamic process at the laboratory scale.

5. Conclusions

The present numerical study proposes a novel multiscale nesting approach within the SPH framework, entirely based on existing numerical tools, to investigate the hydrodynamics arising from the interaction between a propeller jet over a scoured bathymetry at the QES stage and the surrounding flow field characterised by different fluid conditions. Although relying on established numerical capabilities, this approach addresses a class of jet–bathymetry interaction problems that has not yet been systematically explored in the SPH literature. Particular attention is devoted to the definition of the nesting procedure, including the spatial organisation of resolution levels, the treatment of measurement meshes, and the adapted use of relaxation zones, originally conceived for different purposes, which together provide a structured and reproducible methodology with potential relevance for other multiscale SPH applications. To capture the main hydrodynamic features of the investigated processes while limiting computational costs, these complex three-dimensional phenomena have been simulated by coupling a high-resolution near-field domain with a far-field domain characterised by a coarser spatial resolution, representative of laboratory-scale experiments. As a first step, information exchange between the two spatial resolutions has been achieved through a two-dimensional recording mesh used to sample the three-dimensional flow field obtained from the high-resolution simulation. The recorded flow field has then been embedded into the larger domain by means of a relaxation-zone approach, ensuring a smooth and progressive transition between the two regions.

The first case has focused on analysing the PJ flow field in the presence of a steady current, demonstrating the capability of the nesting strategy to reproduce laboratory measurements of the downstream velocity field and the main flow patterns. The computed RI and MI metrics further confirm a good agreement between the SPH simulations and experimental data, particularly in capturing the velocity vector orientation and overall flow structure. Validation of the SPH model has enabled its application to additional scenarios involving PJ interaction under quiescent conditions and in the presence of regular waves, showing that the nesting approach provides an overall good representation of the global characteristics of the velocity magnitude field.

The proposed nesting strategy extends the applicability of SPH to multiscale hydraulic problems and provides a flexible tool for future investigations of fluid–structure and fluid-sediment interaction processes, including erosion prediction, propeller-bed interaction assessment, and the optimisation of marine and fluvial infrastructure design. From a computational standpoint, the proposed nesting strategy offers clear advantages over fully coupled variable-resolution approaches for long-duration simulations over large domains. The propeller-induced flow field is computed once in a dedicated high-resolution simulation and then reused across multiple large-scale configurations, substantially reducing computational cost. Owing to the periodic nature of the propeller-induced flow, the velocity field can be recorded over a limited time window and cyclically imposed in the outer domain, enabling long physical times to be simulated without repeatedly resolving the propeller geometry. In contrast, fully coupled variable-resolution simulations remain computationally prohibitive, as the global time step is dictated by the finest resolution and the per-particle cost increases due to formulation complexity. Within this framework, the nesting strategy provides an efficient multiscale solution. Variable-resolution techniques are instead more effectively employed in the high-resolution propeller-scale simulations, where they can refine the near-field flow and deliver a more accurate velocity field for transfer to larger-scale applications. Nevertheless, it is acknowledged that the current approach presents some numerical trade-offs. The use of a 2D recording mesh inherently filters the finest 3D turbulent structures during information transfer, while the constant-coefficient SPH-LES closure, although ensuring the stability required for long-duration simulations, lacks the local adaptivity of dynamic models. Furthermore, while the adopted momentum-conservative scheme is theoretically susceptible to tensile instability, the combined use of a high-order Wendland kernel and the Fickian-based particle shifting technique provided sufficient regularisation for the propeller-induced jet conditions investigated. Future research will focus on transitioning toward fully coupled variable-resolution frameworks, such as Adaptive Particle Refinement (APR), across the entire computational domain. This evolution, coupled with the implementation of dynamic sub-grid scale closures and advanced TIC algorithms, such as those recently integrated in high-fidelity SPH branches, will aim at resolving the full spectrum of highly anisotropic turbulent flow structures with even higher spatial fidelity, further enhancing the predictive capability of SPH for complex propeller-jet and scoured bed interactions.

Declaration of Generative AI and AI-assisted technologies in the writing process

During the preparation of this work, the authors used ChatGPT 5.2 for language editing. After using this tool, the authors reviewed and edited the content as needed and take full responsibility for the content of the published article.

CRediT authorship contribution statement

D. Ferraro: Writing – original draft, Visualization, Software, Methodology, Investigation, Formal analysis, Data curation, Conceptualization. **J.M. Domínguez:** Writing – original draft, Software, Methodology, Formal analysis, Conceptualization. **A. Lauria:** Validation, Software, Conceptualization. **C. Altomare:** Writing – review & editing, Supervision, Software, Methodology, Conceptualization. **R. Gaudio:** Writing – review & editing, Resources, Project administration, Funding acquisition. **F. Aristodemo:** Writing – original draft, Supervision, Resources, Project administration, Methodology, Funding acquisition, Formal analysis.

Declaration of competing interest

The authors declare that they have no known competing financial interests or personal relationships that could have appeared to influence the work reported in this paper.

Data availability

Data will be made available on request.

References

[1] D. Ferraro, S. Servidio, A. Lauria, R. Gaudio, A local measure of the helicity in turbulent flows, Phys. Fluids 36 (10) (2024).
[2] P. Kumar, K. Mahesh, Large eddy simulation of propeller wake instabilities, J. Fluid Mech. 814 (2017) 361–396.
[3] M. Wei, Y.-M. Chiew, N.-S. Cheng, Recent advances in understanding propeller jet flow and its impact on scour, Phys. Fluids 32 (10) (2020).
[4] M. Albertson, Y. Dai, R.A. Jensen, H. Rouse, Diffusion of submerged jets, Trans. Am. Soc. Civ. Eng. 115 (1) (1950) 639–664.
[5] D. Ferraro, A. Lauria, N. Penna, R. Gaudio, Temporal development of unconfined propeller scour in waterways, Phys. Fluids 33 (9) (2021).
[6] A. Di Mascio, R. Muscari, G. Dubbioso, On the wake dynamics of a propeller operating in drift, J. Fluid Mech. 754 (2014) 263–307.
[7] D. Qin, Q. Huang, G. Pan, P. Han, Y. Luo, X. Dong, Numerical simulation of vortex instabilities in the wake of a preswirl pumpjet propulsor, Phys. Fluids 33 (5) (2021).
[8] R. Muscari, A. Di Mascio, R. Verzicco, Modeling of vortex dynamics in the wake of a marine propeller, Comput. & Fluids 73 (2013) 65–79.
[9] C. Altomare, A.J. Crespo, J.M. Domínguez, M. Gomez-Gesteira, T. Suzuki, T. Verwaest, Applicability of smoothed particle hydrodynamics for estimation of sea wave impact on coastal structures, Coast. Eng. 96 (2015) 1–12.
[10] M. Jandaghian, A. Pilechi, S. Baker, A weakly-compressible SPH-porous media model to simulate wave–breakwater interactions, Coast. Eng. 201 (2025) 104811.
[11] T. Yamamoto, T. Yasuda, K. Oguma, H. Matsushita, Numerical simulation of scattering process of armour blocks on additional rubble mound behind breakwater during tsunami overflow using SPH method, Comput. Part. Mech. 9 (5) (2022) 953–968.
[12] C. Ulrich, M. Leonardi, T. Rung, Multi-physics SPH simulation of complex marine-engineering hydrodynamic problems, Ocean Eng. 64 (2013) 109–121.
[13] D. Ferraro, J.M. Domínguez, A. Lauria, C. Altomare, F. Aristodemo, Smoothed particle hydrodynamics compared to finite volume methods in highly turbulent flow: A three-dimensional analysis of a marine propeller jet case, Phys. Fluids 37 (3) (2025).
[14] D. Ferraro, F. Aristodemo, A. Lauria, E. Lazzaro, D. Pasquali, M. Di Risio, Effect of wave motion on the scouring caused by a marine propeller jet: An experimental and numerical study, Ocean Eng. 290 (2023) 116426.
[15] H. Chen, L. Qian, Z. Ma, W. Bai, Y. Li, D. Causon, C. Mingham, Application of an overset mesh based numerical wave tank for modelling realistic free-surface hydrodynamic problems, Ocean Eng. 176 (2019) 97–117.
[16] D.D. Meringolo, F. Aristodemo, P. Veltri, SPH numerical modeling of wave–perforated breakwater interaction, Coast. Eng. 101 (2015) 48–68.
[17] G. Ruffini, J.M. Dominguez, R. Briganti, C. Altomare, J. Stolle, A.J. Crespo, B. Ghiassi, S. Capasso, P. De Girolamo, MESH-IN: A MESHed INlet offline coupling method for 3-D extreme hydrodynamic events in DualSPHysics, Ocean Eng. 268 (2023) 113400.
[18] F. Ricci, R. Vacondio, A. Tafuni, Multiscale smoothed particle hydrodynamics based on a domain-decomposition strategy, Comput. Methods Appl. Mech. Engrg. 418 (2024) 116500.
[19] F. Ricci, R. Vacondio, J.M. Domínguez, A. Tafuni, Three-dimensional variable resolution for multi-scale modeling in smoothed particle hydrodynamics, Comput. Phys. Comm. 313 (2025) 109609.
[20] Y. Zhan, M. Luo, A. Khayyer, DualSPHysics+: An enhanced DualSPHysics with improvements in accuracy, energy conservation and resolution of the continuity equation, Comput. Phys. Comm. 306 (2025) 109389.
[21] C. Altomare, B. Tagliafierro, J.M. Dominguez, T. Suzuki, G. Viccione, Improved relaxation zone method in SPH-based model for coastal engineering applications, Appl. Ocean Res. 81 (2018) 15–33.
[22] J.M. Domínguez, G. Fourtakas, C. Altomare, R.B. Canelas, A. Tafuni, O. García-Feal, I. Martínez-Estévez, A. Mokos, R. Vacondio, A.J. Crespo, et al., DualSPHysics: from fluid dynamics to multiphysics problems, Comput. Part. Mech. 9 (5) (2022) 867–895.
[23] H. Wendland, Piecewise polynomial, positive definite and compactly supported radial functions of minimal degree, Adv. Comput. Math. 4 (1) (1995) 389–396.
[24] F. Macia Lang, A. Souto Iglesias, M. Antuono, A. Colagrossi, Benefits of using a wendland kernel for free-surface flows, 2011.
[25] G. Fourtakas, J.M. Dominguez, R. Vacondio, B.D. Rogers, Local uniform stencil (LUST) boundary condition for arbitrary 3-D boundaries in parallel smoothed particle hydrodynamics (SPH) models, Comput. & Fluids 190 (2019) 346–361.
[26] G. Fourtakas, R. Vacondio, B.D. Rogers, Divergence cleaning for weakly compressible smoothed particle hydrodynamics, Comput. & Fluids 295 (2025) 106638.
[27] P.N. Sun, A. Colagrossi, S. Marrone, M. Antuono, A.M. Zhang, Multi-resolution delta-plus-SPH with tensile instability control: Towards high Reynolds number flows, Comput. Phys. Commun. 224 (2018) 63–80.
[28] H.G. Lyu, P.N. Sun, X.T. Huang, S.H. Chen, A.M. Zhang, On removing the numerical instability induced by negative pressures in SPH simulations of typical fluid–structure interaction problems in ocean engineering, Appl. Ocean. Res. 117 (2021) 102938.
[29] J. Michel, A. Colagrossi, M. Antuono, S. Marrone, A regularized high-order diffusive smoothed particle hydrodynamics scheme without tensile instability, Phys. Fluids 35 (10) (2023) 103604.
[30] Z. Wang, O.J. Haidn, X. Hu, Efficient implementation of transport velocity formulation, J. Comput. Phys. 538 (2025) 114203.
[31] J. O'Connor, B.D. Rogers, A fluid–structure interaction model for free-surface flows and flexible structures using smoothed particle hydrodynamics on a GPU, J. Fluids Struct. 104 (2021) 103312.
[32] J.J. Monaghan, Smoothed particle hydrodynamics, Annu. Rev. Astron. Astrophys. Vol. 30 (A93-25826 09-90), p. 543-574 30 (1992) 543–574.
[33] R.A. Dalrymple, B.D. Rogers, Numerical modeling of water waves with the SPH method, Coast. Eng. 53 (2–3) (2006) 141–147.
[34] A. Di Mascio, M. Antuono, A. Colagrossi, S. Marrone, Smoothed particle hydrodynamics method from a large eddy simulation perspective, Phys. Fluids 29 (3) (2017) 035102.
[35] D.D. Meringolo, S. Marrone, A. Colagrossi, Y. Liu, A dynamic delta-SPH model: How to get rid of diffusive parameter tuning, Comput. Fluids 179 (2019) 334–355.
[36] H. Gotoh, T. Shibahara, T. Sakai, Sub-particle-scale turbulence model for the MPS method - Lagrangian flow model for hydraulic engineering, Comput. Fluid Dyn. J. 9 (4) (2001) 339–347.
[37] E. Chatzoglou, G. Sofiadis, A. Liakopoulos, Enhancing smoothed particle hydrodynamics for turbulent flow simulation: implementation of the dynamic Smagorinsky model, Eng. Appl. Comput. Fluid Mech. 19 (1) (2025) 2591376.

[38] S.J. Lind, R. Xu, P.K. Stansby, B.D. Rogers, Incompressible smoothed particle hydrodynamics for free-surface flows: A generalised diffusion-based algorithm for stability and validations for impulsive flows and propagating waves, J. Comput. Phys. 231 (4) (2012) 1499–1523.
[39] R. Vacondio, B.D. Rogers, P.K. Stansby, P. Mignosa, J. Feldman, Variable resolution for SPH: a dynamic particle coalescing and splitting scheme, Comput. Methods Appl. Mech. Engrg. 256 (2013) 132–148.
[40] A. English, J.M. Domínguez, R. Vacondio, A.J. Crespo, P.K. Stansby, S. Lind, L. Chiapponi, M. Gómez-Gesteira, Modified dynamic boundary conditions (mDBC) for general-purpose smoothed particle hydrodynamics (SPH): application to tank sloshing, dam break and fish pass problems, Comput. Part. Mech. 9 (5) (2022) 1–15.
[41] A.J. Cabrera Crespo, R. Gómez Gesteira, R.A. Dalrymple, et al., Boundary conditions generated by dynamic particles in SPH methods, Comput. Mater. Contin. (2007).
[42] A. Tafuni, J. Domínguez, R. Vacondio, A. Crespo, A versatile algorithm for the treatment of open boundary conditions in smoothed particle hydrodynamics GPU models, Comput. Methods Appl. Mech. Engrg. 342 (2018) 604–624.
[43] C. Altomare, J.M. Domínguez, A. Crespo, J. González-Cao, T. Suzuki, M. Gómez-Gesteira, P. Troch, Long-crested wave generation and absorption for SPH-based DualSPHysics model, Coast. Eng. 127 (2017) 37–54.
[44] O.S. Madsen, On the generation of long waves, J. Geophys. Res. 76 (36) (1971) 8672–8683.
[45] G. Hamill, C. Kee, D. Ryan, Three-dimension efflux velocity characteristics of marine propeller jets, in: Proceedings of the Institution of Civil Engineers-Maritime Engineering, vol. 168, Thomas Telford Ltd, 2015, pp. 62–75, 2.
[46] W.-H. Lam, G. Hamill, D. Robinson, S. Raghunathan, Observations of the initial 3D flow from a ship's propeller, Ocean Eng. 37 (14–15) (2010) 1380–1388.
[47] D.G. Goring, V.I. Nikora, Closure to "depiking acoustic Doppler velocimeter data" by Derek G. Goring and Vladimir I. Nikora, J. Hydraul. Eng. 129 (6) (2003) 487–488.
[48] P. Frigaard, M. Brorsen, A time-domain method for separating incident and reflected irregular waves, Coast. Eng. 24 (3–4) (1995) 205–215.
[49] E.P. Mansard, E. Funke, The measurement of incident and reflected spectra using a least squares method, in: Coastal Engineering 1980, 1980, pp. 154–172.
[50] T. Wang, W. Li, M. Jia, D. Liu, W. Qin, X. Zhang, Large-eddy simulation of in-cylinder flow in a DISI engine with charge motion control valve: Proper orthogonal decomposition analysis and cyclic variation, Appl. Therm. Eng. 75 (2015) 561–574.
[51] C. Willman, B. Scott, R. Stone, D. Richardson, Quantitative metrics for comparison of in-cylinder velocity fields using particle image velocimetry, Exp. Fluids 61 (2) (2020) 62.
[52] K. Liu, D.C. Haworth, Development and assessment of POD for analysis of turbulent flow in piston engines, in: SAE 2011 World Congress & Exhibition, SAE Technical Paper, 2011.
[53] B. Hu, S. Banerjee, K. Liu, D. Rajamohan, J. Deur, Q. Xue, S. Som, P.K. Senecal, E. Pomraning, Large eddy simulation of a turbulent non-reacting spray jet, in: Internal Combustion Engine Division Fall Technical Conference, vol. 57281, American Society of Mechanical Engineers, 2015, V002T06A007.
[54] M.M. Ameen, Y. Pei, S. Som, Computing statistical averages from large eddy simulation of spray flames, in: SAE 2016 World Congress and Exhibition, SAE Technical Paper, 2016.
[55] L. Skjelbreia, Gravity Waves: Stokes' Third Order Approximation; Tables of Functions, Council on Wave Research, Engineering Foundation, 1959.